

Turbulence and Magnetic Reconnection in Relativistic Multispecies Plasmas

MARIO IMBROGNO ¹, CLAUDIO MERINGOLO ², ALEJANDRO CRUZ-OSORIO ³, LUCIANO REZZOLLA ^{2,4,5},
BENOÎT CERUTTI ⁶, AND SERGIO SERVIDIO ¹

¹*Dipartimento di Fisica, Università della Calabria, Arcavacata di Rende, 87036, Italy*

²*Institut für Theoretische Physik, Goethe Universität, Max-von-Laue-Str. 1, D-60438 Frankfurt am Main, Germany*

³*Instituto de Astronomía, Universidad Nacional Autónoma de México, AP 70-264, 04510 Ciudad de México, Mexico*

⁴*CERN, Theoretical Physics Department, 1211 Geneva 23, Switzerland*

⁵*School of Mathematics, Trinity College, Dublin, Ireland*

⁶*Univ. Grenoble Alpes, CNRS, IPAG, 38000 Grenoble, France*

ABSTRACT

Simulations of relativistic plasmas traditionally focus on the dynamics of two-species mixtures of charged particles under the influence of external magnetic fields and those generated by particle currents. However, the extreme conditions of astrophysical plasmas near compact objects such as black holes and neutron stars are often characterized by mixtures of electrons, protons, and positrons, whose dynamics can differ significantly because of the considerable mass contrast. We present the first two-dimensional particle-in-cell simulations of relativistic turbulence and magnetic reconnection in a three-species plasma, varying the relative abundance of electrons, protons, and positrons while employing realistic mass ratios to achieve unprecedented accuracy. We find that turbulence leads to the formation of magnetic islands, current sheets, and plasmoids. Reconnection occurs between these structures, with plasma composition playing a key role in determining the number of reconnection sites and their energy-conversion efficiency. In particular, as the proton fraction increases, very small-scale features of the turbulence are washed out, while global dissipative effects are amplified. Finally, using a novel generalization of Ohm's law for a relativistic multi-species plasma, we find that the reconnection rate is primarily governed by the electric fields associated to the divergence of the positron and electron pressure tensors. These results provide new insights into dissipation and particle acceleration in turbulent relativistic plasmas, such as those near black holes and neutron stars, and can be used to interpret their high-energy emission and phenomenology.

Keywords: Plasma astrophysics – High energy astrophysics – Space plasmas

1. INTRODUCTION

The study of turbulent relativistic plasmas in astrophysical environments, such as those surrounding black holes and neutron stars, is a crucial research area that integrates high-energy astrophysics, particle kinetics, and magnetohydrodynamics (MHD) (Balbus & Hawley 1998; Blandford & Eichler 1987; Biskamp 2003). These plasmas may consist of multiple particle species, including electrons, protons, and positrons, whose concentrations depend sensitively on the specific astrophysical context. Nevertheless, plasma kinetic effects are essential to accurately capture global behaviors in low-collisionality environments in general, and magnetic reconnection in particular.

Although special- and general-relativistic MHD simulations can reproduce a wide range of reconnection rates in turbulent plasmas (Shibata & Sekiguchi 2005; Giacomazzo & Rezzolla 2007; Anderson et al. 2008; Giacomazzo et al.

2009; Etienne et al. 2015; Liska et al. 2020; Mösta et al. 2013; Porth et al. 2017; Ressler et al. 2021), fluid models are ultimately limited in their ability to describe key kinetic phenomena, such as nonthermal energy distributions and fast magnetic reconnection encountered in astrophysical scenarios (Palenzuela et al. 2009; Yamada et al. 2010; Servidio et al. 2012). In these regimes, kinetic effects are expected to play a dominant role in governing reconnection dynamics.

Arguably, particle-in-cell (PIC) simulations represent the most reliable ab-initio approach for studying the dynamics of free charges under the influence of external magnetic fields and those generated by their currents. However, the vast majority of PIC simulations neglects the presence of positrons (or other ions) and is restricted to simple electron-proton or electron-positron (pair) plasmas. While the inclusion of a third species introduces additional complexity to plasma dynamics, the presence of a third charge carrier can affect local

charge neutrality, current structures, and the efficiency of energy dissipation through reconnection (Sironi & Spitkovsky 2014; Comisso & Sironi 2018). Despite their relevance, the dynamics of fully multi-species configurations remains largely unexplored. Yet, relativistic environments involving accreting compact objects are expected to host not only electrons and protons but also considerable portions of positrons, produced by ultra-high electromagnetic fields accompanying these environments. Typical scenarios where these conditions are met include gamma-ray bursts (Piran 2004; Kumar & Zhang 2015) and pulsar magnetospheres (Harding & Lai 2006; Philippov & Kramer 2022), but also turbulent phenomena such as magnetic breakouts (Most & Quataert 2023; Kiuchi et al. 2024; Musolino et al. 2024), Kelvin-Helmholtz-like instabilities at the jet-disk interface, and regions characterized by magnetic reconnection and plasmoid formation (see, e.g., Nathanail et al. 2020, 2022; El Mellah et al. 2022; Vos et al. 2024). Improving our understanding of these environments is essential for modeling key processes such as jet launching and collimation, large-scale energy transport, and particle acceleration mechanism responsible for high-energy emission (Blandford & Znajek 1977; Blandford & Payne 1982; Murray et al. 1995; Proga et al. 2000; Zenitani & Hoshino 2001; McKinney 2006; Komissarov et al. 2007; Tchekhovskoy et al. 2011; Sironi et al. 2015; Ripperda et al. 2020; Camilloni & Rezzolla 2025).

To overcome these limitations and advance our understanding of particle-field interactions in relativistic environments, we present the first studies of relativistic turbulence using two-dimensional PIC simulations involving three particle species with realistic mass ratios. By systematically varying the positron-to-electron concentration ratio in a globally neutral plasma, we analyze the properties of reconnection regions and show that plasma composition plays a fundamental role in determining both the number of reconnection sites and their dissipation efficiency.

2. METHODS

Simulations are based on a fully kinetic model of relativistic plasma, implemented using the PIC code Zeltron (Cerutti et al. 2013), which solves the equations of motion for a distribution of charged particles coupled to Maxwell's equations. The former are evolved using a standard Boris algorithm (Boris & Shanny 1973), which is second-order accurate, symplectic, and preserves phase-space volume. The latter are expressed in terms of the total magnetic field \mathbf{B} , the electric field \mathbf{E} , the current density $\mathbf{J} := \sum_a q_a n_a \mathbf{V}_a$, and the charge density $\rho_c := \sum_a q_a n_a$. Here, the index a labels the particle species, so that n_a denotes the number density of species a (we use “ p ” for protons, “ $+$ ” for positrons, and “ $-$ ” for electrons), while \mathbf{V}_a and q_a represent the corresponding bulk velocity and charge.

Taking q_- and m_- as the electron charge and mass, respectively, we set $q_- = -q_+ = -q_p = -e$ and $m_- = m_+$, where e is the elementary charge. Under the (reasonable) assumption of global plasma neutrality, the species number densities must satisfy $n_- = n_+ + n_p =: n_0 = (4\pi)^{-1}$. We vary the composition of the three-species plasma through the positron-to-electron concentration ratio, defined as $\chi := n_+/n_-$, which enable us to explore the meaningful physical range

$$\chi = \begin{cases} 0 & \text{if } n_+ = 0; \quad n_- = n_p, \\ 1/2 & \text{if } n_+ = n_p; \quad n_- = 2n_p = 2n_+, \\ 1 & \text{if } n_p = 0; \quad n_- = n_+ \end{cases} \quad (1)$$

where $0 \leq \chi \leq 1$.

The simulation setup follows that discussed by Meringolo et al. (2023), using a computational grid of $N_x = N_y = 8192$ mesh points in a square domain of side length $L_0 \approx 10923 d_-$, where $d_- := c/\omega_{p,-}$ is the electron skin depth, $\omega_{p,-} := \sqrt{4\pi n_0 e^2/m_-}$ the electron plasma frequency, and c the speed of light¹. Importantly, to avoid artifacts and systematic biases, we employ a realistic proton-to-electron mass ratio of $m_p/m_- = 1836$ (see Rowan et al. 2017, for a discussion on the importance of employing realistic mass ratios), and a total of approximately 1.6×10^{10} macroparticles, thereby minimizing noise in both the fields and particle moments.

To accurately simulate multi-species plasmas, it is important to adopt spatial resolutions that capture key physical scales, such as the Debye length and the inverse plasma frequency, while ensuring numerical convergence. At the same time, an optimal balance between computational efficiency and physical accuracy must be maintained. If $\lambda_{D,-} := \sqrt{m_- \theta_- c^2 / 4\pi n_0 e^2}$ denotes the electron Debye length, with θ_- the dimensionless electron temperature, then the spatial and temporal resolutions must be chosen such that $\Delta x < \lambda_{D,-}$ and $\Delta t < (\omega_{p,-})^{-1}$. We set $\Delta x = 4d_-/3 \sim (0.11 - 0.34) \lambda_{D,-}$ (see Tab. 1) and $\Delta t = 0.45 \Delta x = 0.6 (\omega_{p,-})^{-1}$ (see Appendix A for a consistency study). We recall that when particles become relativistic, their skin depth increases proportionally to the square root of the Lorentz factor. Specifically, $d_a^{\text{rel.}} = \sqrt{(\gamma_a m_a c^2) / (4\pi n_a e^2)} = \sqrt{\gamma_a} d_a^{\text{nonrel.}}$, where γ_a denotes the Lorentz factor. Because the average Lorentz factors are $\langle \gamma_- \rangle \sim \langle \gamma_+ \rangle \approx 10 - 10^2$, our resolution is effectively higher than simple non-relativistic considerations may suggest. Moreover, the use of 240 particles per cell (PPC) effectively mitigates noise and guarantees satisfactory accuracy.

¹ Adopting units where $c = 1 = e = m_- = k_B$ implies that $d_- = 1$ as well, where k_B is the Boltzmann constant.

Simulation	χ	β_+	β_p	θ_e	θ_p	$B_{0,z}$	$PP\lambda_{D,-}^2$	$\lambda_{D,-}/\Delta x$	$\lambda_{D,+}/\Delta x$	$\overline{\mathcal{R}}_{\text{XP}}$	ζ
chi.0.1	0.1	1×10^{-2}	9×10^{-2}	137.79	7.50×10^{-2}	52.50	18585	8.80	27.84	0.050	-13.4
chi.0.4	0.4	4×10^{-2}	6×10^{-2}	91.92	5.01×10^{-2}	42.88	12407	7.19	11.37	0.036	-19.4
chi.0.5	0.5	5×10^{-2}	5×10^{-2}	76.63	4.17×10^{-2}	39.15	10359	6.57	9.28	0.031	-20.5
chi.0.6	0.6	6×10^{-2}	4×10^{-2}	61.33	3.34×10^{-2}	35.02	8269	5.87	7.58	0.030	-22.1
chi.0.9	0.9	9×10^{-2}	1×10^{-2}	15.46	8.42×10^{-3}	17.58	2088	2.95	3.11	0.013	-45.6

Table 1. Summary of the parameters for the five simulations presented here. Different simulation setups, labeled as chi.0.1, chi.0.4, chi.0.5, chi.0.6, and chi.0.9, are detailed. From left to right, the columns list: the global positron-to-electron concentration ratio χ ; the plasma beta for positrons (β_+) and protons (β_p) with the electron plasma beta fixed at $\beta_- = 0.1$; the dimensionless temperature for electrons and positrons, $\theta_e = \theta_- = \theta_+$; the out-of-plane magnetic-field strength, $B_{0,z}$; the number of particles per unit area, expressed as $PP\lambda_{D,-}^2$ per unit Debye area; the ratio of the electron and positron Debye lengths to the grid spacing, $\lambda_{D,\pm}/\Delta x$; the median reconnection rate (in absolute value) at X-points, $\overline{\mathcal{R}}_{\text{XP}}$; the slope ζ of the linear fit to the PDFs of the reconnection rates at X-points.

2.1. Generalized Ohm's Law

The interpretation of the simulation results requires a proper understanding of how Ohm's law needs to be modified to account for a system of coupled, charged multi-fluids. In the context of a relativistic electron-positron plasma, such a generalization has been considered, for instance, by [Hesse & Zenitani \(2007\)](#), who examined the role of kinetic dissipation in relativistic magnetic reconnection. In essence, in a relativistic multi-species plasma, Ohm's law, which relates the electric field, plasma currents, anisotropic pressure contributions, and higher-order moments of the distribution function, can be generalized by considering the second moment of the relativistic Vlasov equation and treating separately the terms expressing thermal and kinetic effects. Following a similar methodology, we rewrite the second-order moment of the Vlasov equation (i.e., the momentum-conservation equation) for a given species a as (see Appendix B for details):

$$\partial_t(n_a m_a \mathbf{U}_a) + \nabla \cdot \mathbf{\Pi}_a - q_a n_a (\mathbf{E} + \mathbf{V}_a \times \mathbf{B}) = 0, \quad (2)$$

where \mathbf{U}_a is the bulk four-velocity defined as the density-weighted average of the corresponding four-velocity and representing the first moment of the distribution function, and $\mathbf{\Pi}_a$ is the generalized pressure tensor, which accounts for both thermal and bulk contributions. More specifically, we decompose this tensor by distinguishing the purely thermal contributions, associated with the pressure tensor \mathbf{P}_a , from the kinetic ones as

$$\mathbf{\Pi}_a = \mathbf{P}_a + m_a n_a \mathbf{V}_a \mathbf{U}_a = \int d^3u m_a \frac{\mathbf{u}\mathbf{u}}{\gamma} f_a. \quad (3)$$

In the expression above, $f_a = f_a(\mathbf{x}, \mathbf{u}, t)$ represents the particle distribution function, and $\mathbf{u} := \gamma \mathbf{v}$ denotes the four-velocity of the particles, with \mathbf{v} and γ being the three-velocity and Lorentz factor, respectively. Note that the compact form of the momentum-conservation equation (2) follows from using the continuity equation to cancel the divergence of convective inertia term $\nabla \cdot (m_a n_a \mathbf{V}_a \mathbf{U}_a)$ with the corresponding contribution arising from the divergence of the pressure tensor \mathbf{P}_a .

After combining the contributions from all three species considered, the resulting expression for the electric field defines the generalized Ohm's law for a three-species relativistic plasma, given by:

$$\begin{aligned} \mathbf{E} = & \frac{m_-}{e^2 \mathcal{N}} \partial_t \mathcal{J} - \frac{1}{\mathcal{N}} (n_+ \mathbf{V}_+ + n_- \mathbf{V}_-) \times \mathbf{B} \\ & - \frac{1}{\mathcal{N}} n_p \mathbf{V}_p \times \mathbf{B} - \frac{1}{e \mathcal{N}} \nabla \cdot \mathbf{\Pi}_- \\ & + \frac{1}{e \mathcal{N}} \nabla \cdot \mathbf{\Pi}_+ + \frac{m_-}{m_p} \frac{1}{e \mathcal{N}} \nabla \cdot \mathbf{\Pi}_p \\ = & \mathbf{E}_{\partial_t} + \mathbf{E}_{vb\pm} + \mathbf{E}_{vbp} + \mathbf{E}_{\Pi-} + \mathbf{E}_{\Pi+} + \mathbf{E}_{\Pi p}, \end{aligned} \quad (4)$$

where $\mathcal{N} := n_p m_- / m_p + n_+ + n_-$ is the total effective number density, $\mathcal{J} := \sum_a q_a n_a \mathbf{U}_a$ represents the current density associated with the bulk four-velocity, and the different terms in the last line of Eq. (4) correspond to those appearing on the right-hand side.

Expression (4) offers a concise yet comprehensive description of the six different contributions to the electric field in a relativistic three-species plasma. To the best of our knowledge, this is the first time that an expression for a relativistic three-species Ohm's law has been presented. As we discuss below, each term can be monitored and characterized to support the interpretation of our simulation results.

2.2. Initial Conditions

Assuming a Cartesian coordinate system where the plasma dynamics unfolds in the (x, y) plane, we establish a strongly turbulent regime by initializing a large-scale, random magnetic field determined via a superposition of low-wavenumber Fourier modes ([Meringolo et al. 2023](#); [Meringolo et al. 2024](#)), combined with a uniform background magnetic field directed along the z -direction $B_{0,z}$. More specifically, the initial magnetic field configuration is such that $\langle B_{xy} \rangle_{\text{rms}} / B_{0,z} \sim 1$ ([Servidio et al. 2012](#)), where $\langle \delta B_{xy} \rangle_{\text{rms}}$ represents the root-mean-square (rms) fluctuations of the in-plane magnetic field.

After defining the total enthalpy density as $\rho h = \rho + \mathcal{U} + p$, where $\rho := \sum_a n_a m_a c^2$ is the (total) rest-mass density,

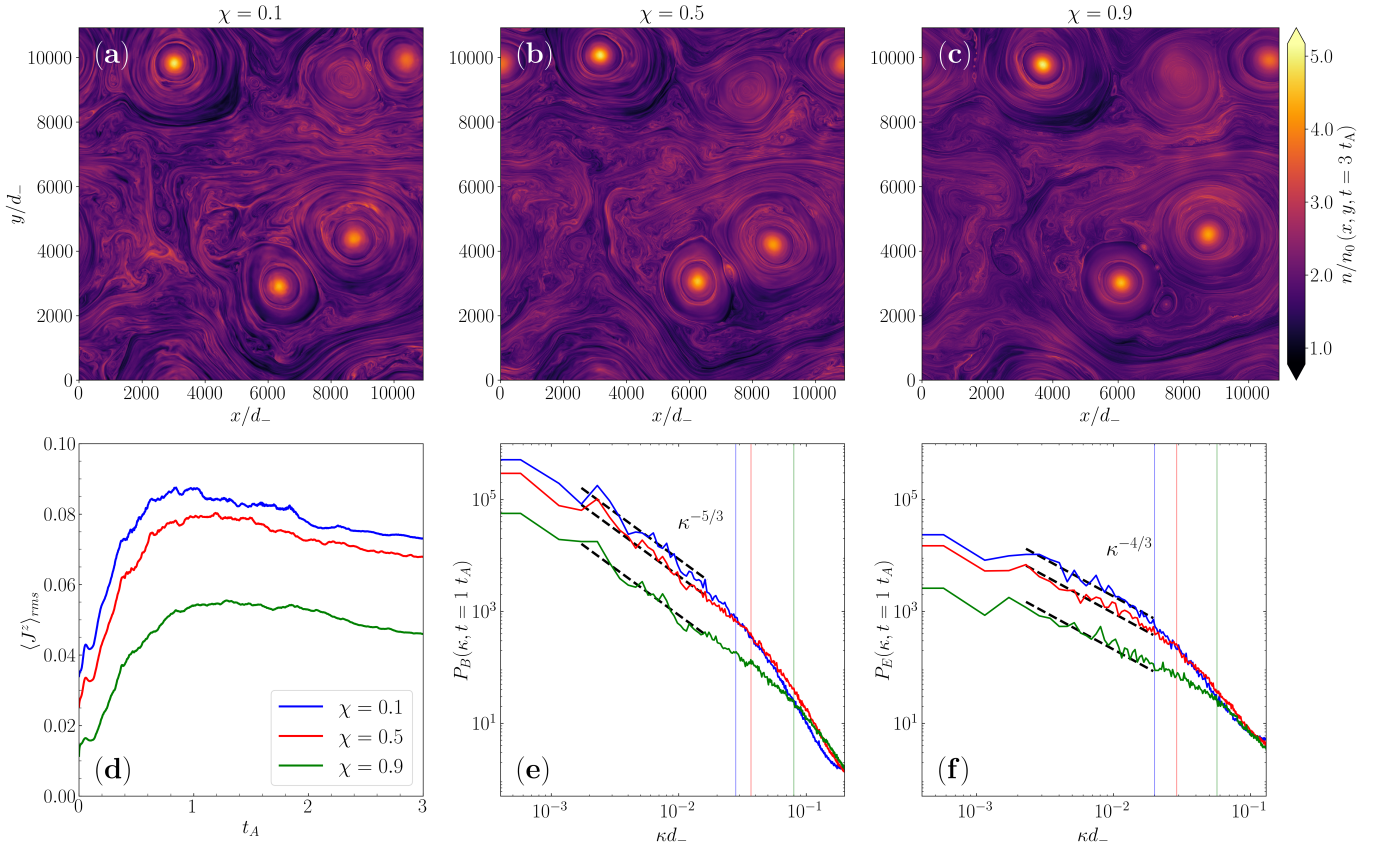


Figure 1. Upper row: Snapshots of the (normalized) total number density $n/\langle n \rangle_{\text{rms}}$ at time $t = 3 t_A$ for $\chi = 0.1$ (a), $\chi = 0.5$ (b), and $\chi = 0.9$ (c). Lower row: Panel (d) shows the evolution of the rms of the out-of-plane component of the current density for different concentration ratios; (e) shows the power spectrum of the magnetic field when turbulence is fully developed at $t = 3 t_A$, with the corresponding slopes; (f) shows the same as in (e), but for the electric field. The power spectra are normalized to the rms of the in-plane magnetic field. Thin solid lines mark the spectral slope breaks in the inertial range.

$\mathcal{U} \approx \sum_a p_a (\Gamma_a - 1)^{-1}$ the internal energy density, and $p := \sum_a p_a$ the total pressure (Rezzolla & Zanotti 2013), we introduce the magnetization parameter $\sigma := p_{\text{mag}}/\rho h = B^2/\rho h$ to distinguish between regions that are magnetically dominated (i.e., $\sigma \gg 1$) and those that are not (i.e., $\sigma \lesssim 1$). A couple of remarks should be made. First, alternative definitions of magnetization exist that involve only the rest-mass density (see, e.g., Porth et al. 2019). Second, although our plasma is collisionless, we model it using an ideal-gas equation of state (Rezzolla & Zanotti 2013) with an adiabatic index Γ_a for each species; as customary, we set $\Gamma_a = 4/3$ for all species (Ball et al. 2018). Similarly, we introduce the total plasma beta parameter, $\beta := \sum_a \beta_a$, as the ratio of plasma to magnetic pressure, where $\beta_a := 8\pi n_a k_B T_a / B_{0,z}^2 = 8\pi n_a \theta_a m_a c^2 / B_{0,z}^2$, and T_a is the effective temperature of each species.

We note that, despite the numerous degrees of freedom in our setup, it is possible to construct a controlled set of simulations in which the role of the concentration ratio χ can be isolated by keeping β , σ , and the turbulence levels $\langle B_{xy} \rangle_{\text{rms}}/B_{0,z}$ fixed. In this way, we simulate five different plasma configurations, each regulated by different values of

χ (see Tab. 1 for a summary of the key properties), explore the dynamics of a three-species trans-relativistic plasma, and assess the implications for relativistic astrophysical plasmas around compact objects².

Since σ and β determine the main properties of the plasma and its dynamics, our initial conditions for the magnetization and plasma beta are inspired from GRMHD simulations of accretion flows onto black holes (Porth et al. 2019; Nathanail et al. 2020; Ripperda et al. 2020; Nathanail et al. 2022; Meringolo et al. 2023). Hence, we set $\beta \approx 0.2$ (with $\beta_- \approx 0.1$) and $\sigma \approx 1$. This choice ensures a balance between magnetic and kinetic forces, facilitating characteristic plasma behaviors such as vortex formation and magnetic stability, while still allowing for instabilities to develop. In this weakly relativistic regime, often referred to as “trans-relativistic”, protons remain non-relativistic, while electrons and positrons exhibit a relativistic behavior (see Ball et al. 2018, for a proton-electron plasma in this regime).

² Due to the considerable mass difference, B_0 needs to be adjusted for different values of χ to preserve constant values of σ and β .

Hereafter, and for compactness, we focus on a detailed discussion of three representative configurations (i.e., $\chi = 0.1, 0.5$, and 0.9), with the results from the other setups falling in between those presented.

3. RESULTS

3.1. Turbulence and Dissipation

Given the chosen initial conditions, turbulence develops very rapidly and saturates after approximately one Alfvén time $t_A := L_0/v_A$, where $v_A := c\sqrt{\sigma/(1+\sigma)}$ is the Alfvén speed. After this time, the system reaches a quasi-steady state, as indicated by the saturation of the rms of the out-of-plane (z) component of the total current, J^z , as shown in Fig. 1-(d). Once turbulence is fully developed, magnetic islands begin to merge - regions of confined magnetic flux (see also below) - leading to an inverse cascade of magnetic helicity and the generation of long-lived, large-scale structures (Imbrogno et al. 2024). These large-scale islands are illustrated in panels (a)–(c) of Fig. 1, which show the total number density at $t = 3t_A$. Note that as χ decreases (and, consequently, the proton number density increases), very small-scale features are washed out (i.e., only the largest anisotropies persist) and dissipative effects become more pronounced. This response is quantified by the total rms out-of-plane current $\langle J^z \rangle_{\text{rms}}$ [Fig. 1-(d)], which is smaller for increasing values of χ . A similar trend can also be inferred in terms of plasmoid formation. In particular, as $\chi \rightarrow 1$, corresponding to a pure pair-plasma configuration, the elongated current sheets between magnetic islands become unstable and break up at what we refer to as “X-points” (see below for a definition), forming sequences of plasmoids that are subsequently accelerated (Bessho & Bhattacharjee 2005; Sironi et al. 2016) [see Fig. 1-(c)].

Panels (e) and (f) of Fig. 1 report the spectra of the magnetic and electric fields at $t = 3t_A$ for the three representative mixtures. The slopes observed over approximately one decade in normalized wavenumber, κd_- , indicate that the magnetic power spectrum is steeper, scaling as $\propto \kappa^{-5/3}$, compared to the electric power spectrum, which scales as $\propto \kappa^{-4/3}$. While the former scaling matches the expectations for fully developed isotropic turbulence, the latter likely contains additional electric-field contributions arising from anisotropic stresses beyond the ideal-MHD approximation. Similar scalings have also been reported in non-relativistic turbulence (González et al. 2019) and magnetic reconnection (Adhikari et al. 2023; Lewis et al. 2023). Notably, these behaviors align with several studies of solar-wind turbulence (Bale et al. 2005; Alexandrova et al. 2009; Sahraoui et al. 2009). It is also worth remarking that the scales at which the turbulent cascades are cut off vary with the mixture composition. Specifically, at these resolutions, the cut-off shifts to smaller scales, down to $\kappa d_- \lesssim 0.08$ when $\chi \rightarrow 1$,

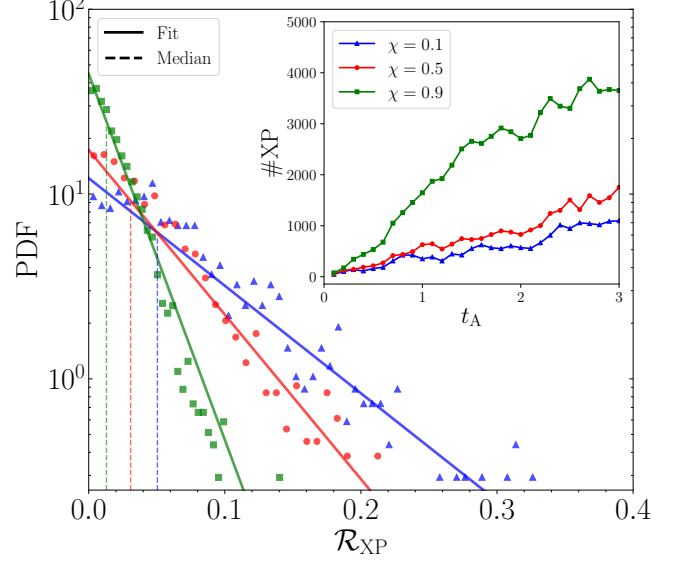


Figure 2. PDFs of the reconnection rates (symbols) for $\chi = 0.1$ (blue), $\chi = 0.5$ (red), and $\chi = 0.9$ (green), with corresponding linear fits shown as solid lines in matching colors. Dashed vertical lines indicate the median reconnection rates for each distribution, while the inset shows the evolution of the number of X-points ($\#XP$) for each configuration.

while larger scales, up to $\kappa d_- \lesssim 0.02$, are suppressed when $\chi \rightarrow 0$ (see colored vertical lines). The loss of power at large κ 's begins earlier for $\chi = 0.1$ than for $\chi = 0.9$, indicating that the presence of protons is effectively associated with the “washing out” of turbulence at the smallest scales.

3.2. X-points, Electric fields, and Reconnection Rates

Because X-points play a particularly important role in astrophysics, we have focused on their occurrence in our simulations and the analysis of various physical quantities at these locations. In particular, at any given time, we compute the Hessian matrix of the z -component of the vector potential, $A^z(x, y)$, defined as $H_{i,j}^{A^z}(\mathbf{x}) := \partial^2 A^z / \partial x_i \partial x_j$. At each neutral point, where $\nabla A^z \times \mathbf{e}_z = 0$, we evaluate the local eigenvalues and eigenvectors of $H_{i,j}^{A^z}$ (see Servidio et al. 2010, for details on the implementation in the presence of a stochastic field). We then classify the neutral point as an X-point if it is a saddle point, or as a magnetic island if it corresponds to an extremum (Servidio et al. 2009). Using this technique, we identify $\sim 10^2$ X-points in the very early stages of the simulation, with their number increasing over time and as a function of χ (see inset in Fig. 2).

Having isolated X-points and magnetic islands, we were able to separately assess the role of the different contributions to the electric field in a three-species plasma, as described by Eq. (4). The corresponding results are shown in the top panel of Fig. 3, which displays the probability distribution function (PDF) of the various terms contributing to the z -component of the electric field at $t = 3t_A$, computed over the entire do-

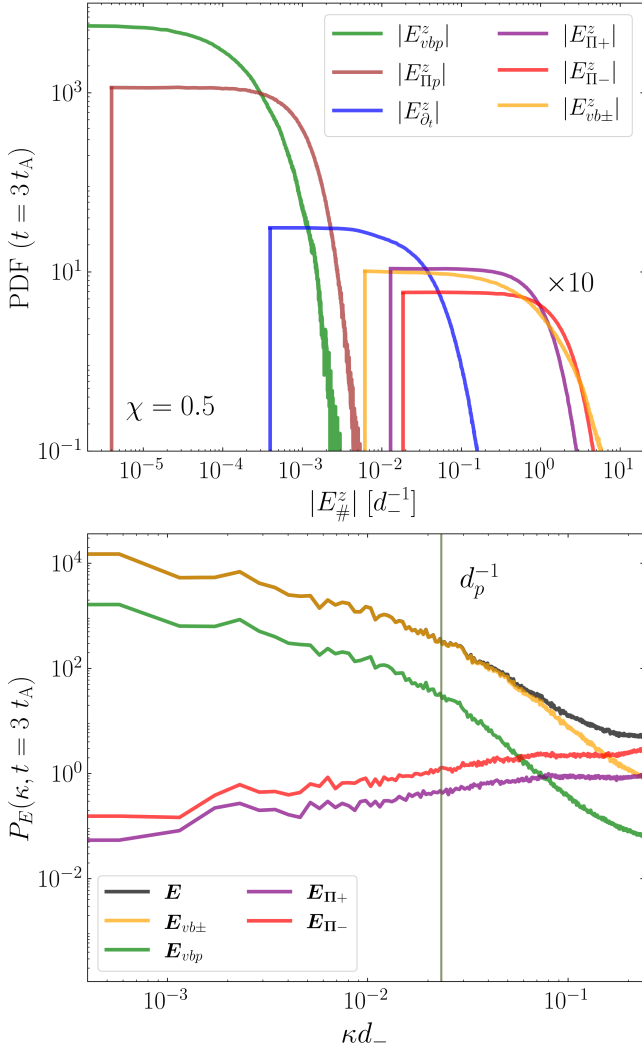


Figure 3. *Top panel:* PDFs of the various contributions to the electric field in the z -direction, as given in Eq. (4), for $\chi = 0.5$ and at $t = 3 t_A$. *Bottom panel:* Power spectra of the dominant contributions reported in the top panel. Marked with the gray vertical line is the typical proton scale.

main for the case with $\chi = 0.5$ (see Fig. A2 in Appendix C for the behavior at different concentrations). Note that some components have been amplified by a factor of ten to be visible on the same scale. A quick inspection of Fig. 3 reveals that the largest electric-field contribution comes from what we refer to as the “proton-induced electromotive-force” term, E_{vbp}^z (green line), followed by the proton pressure-gradient term, $E_{\Pi p}^z$ (brown line). Interestingly, a sizeable contribution is also provided by the displacement term of the momentum current density, $E_{\partial_t}^z$ (blue line), consistent with the findings of Hesse & Zenitani (2007) in the presence of a guide magnetic field. Note that although these electric fields are quite common, they are also very weak and at least three orders of magnitude weaker than the other electric-field contributions,

such as $E_{\Pi-}^z$, $E_{\Pi+}^z$, and $E_{vb\pm}^z$, which are four orders of magnitude less common.

The bottom panel of Fig. 3 provides the spectral distribution of the various components of the electric field, revealing that at small scales the component $E_{vb\pm}$ becomes less dominant, despite being primarily responsible for the overall large-scale behavior of the total electric field. In contrast, the components $E_{\Pi-}$ and $E_{\Pi+}$ contribute most significantly at small scales. In fact, at the smallest scales resolved by our simulation and for $\chi = 0.5$, we find $P_{E_{\Pi-}} \sim P_{E_{vb\pm}}$. Overall, Fig. 3 presents a comprehensive and intriguing picture of the electric-field distribution, highlighting a landscape where weak but frequent electric fields coexist with strong yet rare ones. The implications of this complex structure will be explored in detail in a separate work (Meringolo et al. 2025).

Since X-points coincide with reconnection sites, we use our time-dependent map of their location and distribution to calculate the reconnection rate as

$$\langle \mathcal{R}_{XP} \rangle := \langle |E^z(XP)| / \langle B_{xy} \rangle_{\text{rms}} \rangle, \quad (5)$$

namely, the average of the ratio of the z -component of the electric field at the X-point to the rms of the in-plane magnetic field, expressed in units of the speed of light (Zenitani & Hoshino 2001; Kagan et al. 2015; Liu et al. 2015; Uzdensky & Loureiro 2016).

Figure 2 illustrates the PDFs of the reconnection rates for all of the X-points across the whole computational domain and the three reference cases, along with their respective linear fits. Although the data exhibit significant variance, they suggest that lower values of χ leads to higher median reconnection rates (vertical dashed lines). Furthermore, the median reconnection rate demonstrates a clear linear dependence on the mixture composition, which can be approximated as $\overline{\mathcal{R}}_{XP} \approx a_1(1 - \chi)$, with $a_1 \approx 0.06 \pm 0.0004$ (see also Tab. 1). The inset in Fig. 2 displays the time evolution of the number of X-points for the three plasma species. Interestingly, the nearly pure pair plasma ($\chi = 0.9$) produces almost three times as many X-points as plasmas containing a fraction of protons, with their number continuing to increase over time. In contrast, the nearly pure electron-proton plasma ($\chi = 0.1$) yields the lowest number of X-points, with the latter remaining relatively stable throughout the evolution. At the same time, the $\chi = 0.1$ plasma also leads to extreme reconnection processes with $\mathcal{R}_{XP} \simeq 0.4$, which, albeit rare, may be responsible for the most interesting astrophysical phenomenology such as coronal mass ejections. We should also note that the inclusion of positrons significantly alters the dynamics of classical proton-electron plasmas, disrupting the current layers and weakening local reconnection processes and dramatically changing the reconnection rate. Hence, while in the limit $\chi \rightarrow 1$ protons are absent, the electron-positron plasma that is produced in this

case is very different from a pure-electron plasma (Phan et al. 2018; Sharma Pyakurel et al. 2019). The latter is much closer to an idealized plasma and thus exhibits a rather large reconnection rate. Additional key quantities related to the reconnection rates as a function of χ , including the averages of their absolute values and the slopes of the linear fits shown in Fig. 2, are summarized in Tab. 1.

In addition to the global statistical overview presented in Fig. 2, we also investigate the behavior of the electric and magnetic fields at X-points. To gain insight into the most intense reconnection sites, we consider the “strongest” X-points, namely those for which the reconnection rate exceeds a threshold, $\mathcal{R}_{\text{XP}} > \mathcal{R}_{\text{XP,th}}$, where $\mathcal{R}_{\text{XP,th}}$ is defined as one standard deviation above the median. For the cases with $\chi = 0.1, 0.5$ and 0.9 , the corresponding thresholds are $\mathcal{R}_{\text{XP,th}} = 0.12, 0.08$, and 0.03 , respectively. These locations, representing $\approx 18\%$ of the total X-points, are analyzed by evaluating one-dimensional averages of the magnetic field components tangent (\hat{t} ; blue arrows in the left panel of Fig. 4) and orthogonal to the current sheet (\hat{n} ; red arrows), i.e., $B_{\hat{n}}$ and $B_{\hat{t}}$, respectively [panels (a), (c), and (e) of Fig. 4], as well as the electric-field components $E_{\Pi-}^z$ and $E_{\Pi+}^z$, noticing that the convective electric field component $E_{vb\pm}^z$ vanishes at any X-point [panels (b), (d), and (f) of Fig. 4].

As shown in panels (a), (c), and (e) of Fig. 4, the magnetic field component perpendicular to the current sheet ($B_{\hat{n}}$) changes sign at the X-point, while the tangential component ($B_{\hat{t}}$) remains zero, in agreement with the Sweet-Parker model (Parker 1957). Similarly, panels (b), (d), and (f) illustrate that all the averaged electric field contributions peak at the X-point, with the electron pressure-gradient term $E_{\Pi-}^z$ being the dominant one. As χ increases, the electric field associated with the positron pressure-gradient, $E_{\Pi+}^z$, also grows, becoming comparable to $E_{\Pi-}^z$ when $\chi = 0.9$. These two terms emerge as the dominant contributions to the electric field in these regions, directly governing the reconnection process and acting as the main drivers of particle acceleration.

This behavior is not difficult to interpret: when $\chi = 1$ (i.e., when no protons are present), the electric fields arising from the pressure gradients of electrons and positrons contribute equally. However, when $\chi < 1$ (i.e., when protons are present), the electric fields from positron pressure-gradients compete with those from protons and become less dominant, causing differences in acceleration between electrons and positrons to emerge.

To quantify how the electric fields related to pressure-gradient terms differ as χ changes, we computed the ratio $E_{\Pi+}^z/E_{\Pi-}^z$ at the X-points for different values of χ . We found that this ratio can be approximated by the fitting expression $E_{\Pi+}^z/E_{\Pi-}^z \approx 0.4\chi^2 + 0.6\chi$. Clearly, the ratio

$E_{\Pi+}^z/E_{\Pi-}^z \rightarrow 0$ when no positrons are present ($\chi \rightarrow 0$), while $E_{\Pi+}^z/E_{\Pi-}^z \rightarrow 1$ for a pure pair plasma ($\chi \rightarrow 1$).

4. CONCLUSIONS

Using accurate PIC simulations, we have conducted a systematic analysis of turbulent relativistic plasmas comprising three species of charged particles: electrons, positrons, and protons with a realistic mass ratio. This study represents a significant step towards modeling astrophysical plasmas around compact objects, where all three species are expected to coexist. By systematically varying the positron-to-electron concentration ratio, χ , we have progressively explored how the presence of positrons alters not only the spectral properties of turbulent plasmas but also how the relative concentrations of the three species affect the formation of magnetic islands, current sheets, and plasmoids.

More specifically, by performing five long-term simulations with a varying mixture from $\chi = 0.1$ (corresponding to a vanishing positron fraction) to $\chi = 0.9$ (corresponding to a vanishing proton fraction), we have highlighted that as χ increases, smaller-scale features in the turbulence are gradually washed out (i.e., only the largest anisotropies persist) and global dissipative effects (i.e., across all scales) are increased. This behavior can be quantified in three different ways. First, by analyzing the total rms out-of-plane current $\langle J^z \rangle_{\text{rms}}$, which decreases as χ increases. Second, by examining the spectral properties of the turbulent electric and magnetic fields, which, for small values of χ , exhibit significant higher powers at small scales and an earlier departure from a power-law scaling. Lastly, by considering the PDFs of the reconnection rate measured at the X-points, which clearly show a decrease in median values as χ increases.

Overall, these systematic variations in the turbulent and dissipative phenomenology resulting from the changes in charge composition suggest that the presence of more protons leads to less frequent but more energetic reconnection events, with larger reconnection rates. In turn, dissipation occurs primarily at the smallest scales, disrupting the clear power-law scaling, while the largest turbulent structures remain unaffected. By contrast, pure electron-positron plasmas are characterized by more frequent but less energetic reconnection events, leading to comparatively lower reconnection rates. As a result, dissipation takes place at all scales, preserving a clear power-law scaling.

A considerable effort has also been dedicated to defining the generalization of Ohm’s law for a three-species plasma, which provides a relationship between the electric field, plasma currents, anisotropic pressure contributions, and higher-order moments of the distribution function. In this way, it was possible to disentangle the large-scale contributions of the electromotive force from the small-scale contributions associated with the gradients of the pressure ten-

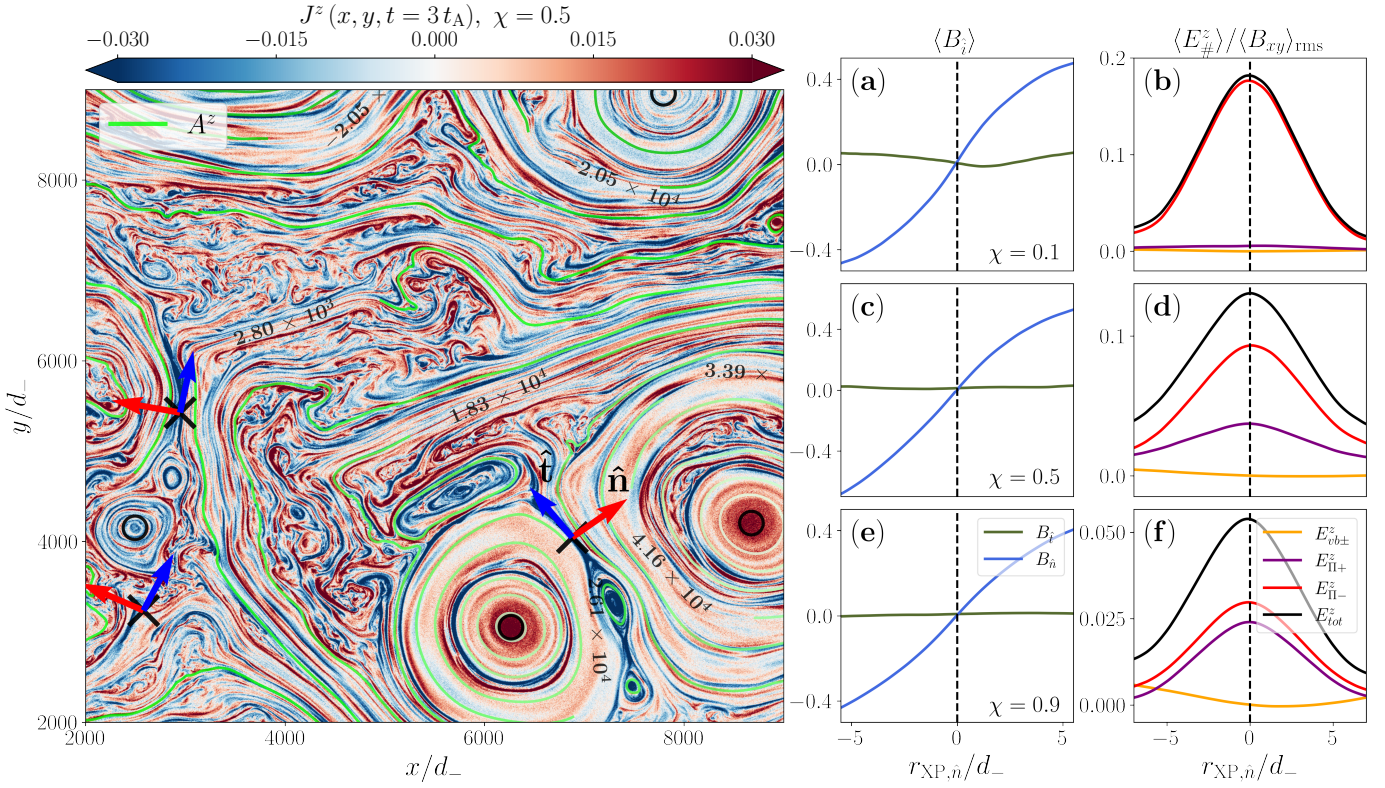


Figure 4. *Left panel:* colormap of the current density in the z -direction at $t = 3t_A$ for the simulation with $\chi = 0.5$. Bright green lines indicate isocontours of the out-of-plane component of the vector potential A^z . Several strong X-points are marked with an \times and serve as origin for the normal and tangent unit vectors \hat{n} (red arrows) and \hat{t} (blue arrows), respectively. *Right panels:* the left column shows the average profiles of the magnetic-field components parallel (blue lines) and perpendicular (gray lines) to the current sheet, plotted along the n -direction, for $\chi = 0.1$ (top row), $\chi = 0.5$ (middle row), and $\chi = 0.9$ (bottom row). The right column displays the average profiles of the various contributions to Ohm's law, including the total electric field (black lines), the positron pressure-gradient contribution (purple lines), the electron pressure-gradient contribution (red lines), and the electron-positron electromotive contribution (orange lines), also along the n -direction. As before, each row correspond to a different value of χ .

sor. More specifically, at the X-points, where reconnection occurs, the electromotive terms vanish, and the only contributions to the electric field arise from the pressure gradients, primarily those from electrons and positrons (the pressure-gradient term associated with protons is negligible because of their larger mass). As a result, for large values of χ , the pressure contributions from electrons and positrons are comparable, and the reconnection is mediated by multi-plasmoids, leading to weaker reconnection rates. By contrast, for small values of χ , the electron pressure term is dominant and small-scale plasmoids are less frequent, resulting in more energetic reconnection events.

While a full comprehension of this behavior will require additional studies, a possible explanation is as follows. In the limit $\chi \rightarrow 0$, i.e., for an equal mixture of electrons and protons, the substantial mass difference between the two will lead to different currents in the two species and to a smaller total current. Within a turbulent reconnection scenario, this will translate into a small number of X-points, but also into a larger reconnection rate because these X-points will have a smaller number density and can generate a larger dissipa-

tion. On the other hand, in the limit $\chi \rightarrow 1$, i.e., for an equal mixture of electrons and positrons, the latter will be much more “mobile”, leading to comparable currents in the two species and to a larger total current. In addition, because in our simulations the magnetization σ is kept constant, the initial (and subsequent) magnetic field is smaller for the e^-e^+ mixture (see Tab. 1). Using Eq. (5), $\mathcal{R}_{\text{XP}} \sim E^z/B_{xy} \sim J_{xy}B_{xy}/(enB_{xy}) \sim (\nabla \times B)_{xy}/(en) \sim B_{0,z}/(en\mathcal{L})$, where \mathcal{L} is a characteristic lengthscale for the current sheet. It follows that $\mathcal{R}_{\text{XP}}|_{\chi \rightarrow 0}/\mathcal{R}_{\text{XP}}|_{\chi \rightarrow 1} \sim B_{0,z}|_{\chi \rightarrow 1}/B_{0,z}|_{\chi \rightarrow 0} \sim 3$ (see Tab. 1) if we assume that the thickness of the current sheet \mathcal{L} is not very different in the two cases. Such a ratio of the reconnection rate that we have estimated in this way is similar to what is shown in Fig. 3. Stated differently, in general we expect that the reconnection rate will decrease with the increase of χ as the addition of positrons will “pollute” any plasma mixture. As a result, in the electron-positron mixture relative to $\chi = 0.9$, the number of X-points will increase, but because of the reduced magnetic field they will have a smaller reconnection rate and be responsible for a smaller dissipation.

Although our results offer an approach to studying and understanding relativistic multi-species plasmas, several improvements are possible. First, extending the simulations to three spatial dimensions would allow us to assess how the plasmoid phenomenology, which is known to change in three dimensions (see, e.g., [Nathanail et al. 2022](#)), affects the conclusions drawn here. Second, it would be valuable to determine how high-curvature spacetimes influence the inertial effects of charged particles. Finally, while the spatial and particle resolutions employed in this study are sufficient for drawing robust conclusions, higher resolutions are necessary to further explore the spectral properties of the turbulent plasma. We plan to address these aspects in future work.

ACKNOWLEDGEMENTS

It is a pleasure to thank F. Camilloni for useful discussions. This research is supported from the European Union’s Horizon Europe research and innovation programme under grant agreement No. 101082633 (ASAP), the ERC Ad-

vanced Grant “JETSET: Launching, propagation and emission of relativistic jets from binary mergers and across mass scales” (Grant No. 884631), and the ERC Consolidator Grant SPAWN (Grant No. 863412). A.C.O acknowledges to the DGAPA-UNAM (grant IN110522), the “Ciencia Básica y de Frontera 2023–2024” program of SECIHTI México (projects CBF2023-2024-1102 and 257435). L.R. acknowledges the Walter Greiner Gesellschaft zur Förderung der physikalischen Grundlagenforschung e.V. through the Carl W. Fueck Laureatus Chair and the hospitality at CERN, where part of this research was carried out. Computational resources were provided by CINECA through the ISCRA Class B project “KITCOM-HP10BB7U73”. We acknowledge ISCRA for awarding this project access to the LEONARDO supercomputer, owned by the EuroHPC Joint Undertaking, hosted by CINECA (Italy). Simulations were also performed on HPE Apollo HAWK at the High Performance Computing Center Stuttgart (HLRS) under the grant BNSMIC, on the Goethe-HLR supercomputer, on the local supercomputing cluster Calea, and on the Alarico HPPC Computing Facility at the University of Calabria.

APPENDIX

A. CONSISTENCY STUDY

As discussed in the main text, choosing a resolution of $\Delta x = 4/3 d_{e-}$ does not fully resolve the electron skin depth. To verify that this choice does not compromise the validity of our results, we perform a convergence study of the particle distribution functions across multiple configurations with varying grid spacings, while keeping the physical box length fixed at $L_0 = 5461.33 d_{e-}$. Specifically, we analyze the following resolutions

$$\begin{aligned}
 \Delta x &= (1/3) d_{e-}, N_x = N_y = 16384, \text{ PPC} = 15, \\
 \Delta x &= (2/3) d_{e-}, N_x = N_y = 8192, \text{ PPC} = 60, \\
 \Delta x &= (4/3) d_{e-}, N_x = N_y = 4096, \text{ PPC} = 240, \\
 \Delta x &= (8/3) d_{e-}, N_x = N_y = 2048, \text{ PPC} = 960, \\
 \Delta x &= (16/3) d_{e-}, N_x = N_y = 1024, \text{ PPC} = 3840.
 \end{aligned}
 \tag{A1}$$

where PPC indicates the number of particles per cell.

Concentrating for convenience on the case with $\chi = 0.5$, the results of this consistency analysis are summarized in Fig. A1, which reports the particle kinetic-energy distributions (with the rest-mass energy subtracted) expressed as function of the Lorentz factor for electrons (left panel), positrons (middle panel), and protons (right panel), along with the numerical setups detailed in (A1). Clearly, all distributions are very similar to each other, especially at the highest energies. This confirms that a resolution of $\Delta x =$

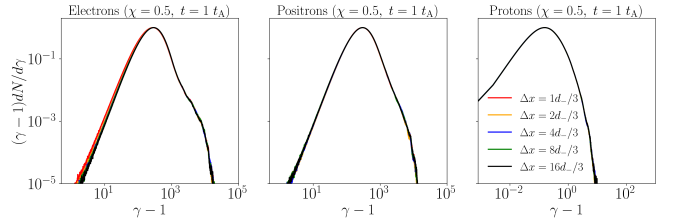


Figure A1. Consistency study showing the particle kinetic-energy distributions expressed as a function of the Lorentz factor for electrons (left panel), positrons (middle panel), and protons (right panel). The simulations refer to the case with $\chi = 0.5$ and show the different setups listed in (A1) at $t = t_A$.

$(4/3) d_{e-}$ is sufficient for our purposes, as it does not violate the main PIC constraints outlined in the core of the paper and provides a sufficient number of PPC to contrast and limit noise.

Another important consistency check in our simulations is provided by combining together all the different electric-field components in the last line of Ohm’s law in Eq. (4), and that we compute separately, and to ensure that they actually lead to the same total electric field computed in the simulation. This is shown in Fig. A2, which reports the PDFs of the modulus of the electric field $|\mathbf{E}|$ at time $t = 3 t_A$ as computed by the aggregation of the various components ($|\mathbf{E}_{\text{Ohm}}|$, black line) or by the total electric field of the simulation ($|\mathbf{E}_{\text{sim}}|$, red line). The different panels, which refer to $\chi = 0.1$ (left),

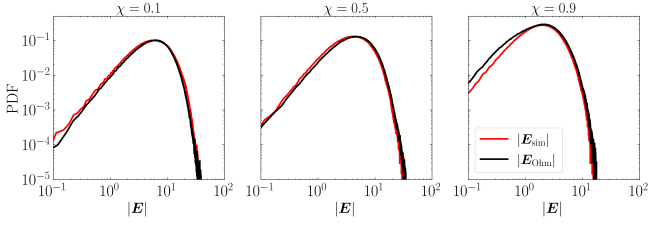


Figure A2. PDFs of the modulus of the electric field $|\mathbf{E}|$ at time $t = 3 t_A$ as computed by the aggregation of the various components ($|\mathbf{E}_{\text{Ohm}}|$, black line) or by the total electric field of the simulation ($|\mathbf{E}_{\text{sim}}|$, red line). The different panels, refer to $\chi = 0.1$ (left), $\chi = 0.5$ (middle) $\chi = 0.9$ (right).

$\chi = 0.5$ (middle) $\chi = 0.9$ (right) clearly show that the different contributions reconstruct very accurately the total electric field; small differences appear for the case with $\chi = 0.9$ but only in the weakest fields, while the larger ones are reproduced very accurately. We expect this deviation to be linked to the electric-field contribution $\mathbf{E}_{\partial t} \propto \partial_t \mathcal{J}$, which is not well-captured on the largest scales as the number of positron increases with χ (see also Hesse & Zenitani 2007). Overall, the results in Fig. A2 provide us with important confidence on our ability to track down the single contributions to Ohm's law.

B. ON THE GENERALIZED OHM'S LAW

We here provide additional details on the derivation of the generalized Ohm's law of a three-species relativistic plasma, Eq. (4) reported in the main text. As customary, we start from the relativistic Vlasov equation, governing for each species a the evolution of the corresponding distribution function f_a and taking the form [see Chap. 2 in Cercignani et al. (2002) or Chap. 6 in Liboff (2003)]

$$\partial_t f_a + \frac{\mathbf{u}}{\gamma} \cdot \nabla f_a + \frac{q_a}{m_a} \left(\mathbf{E} + \frac{\mathbf{u} \times \mathbf{B}}{\gamma} \right) \cdot \frac{\partial f_a}{\partial \mathbf{u}} = 0, \quad (\text{B2})$$

where $f_a = f_a(\mathbf{x}, \mathbf{u}, t)$ is the particle distribution function, $\mathbf{u} = \gamma \mathbf{v}$ the four velocity, with \mathbf{v} the three-velocity and $\gamma := (1 - v^2)^{-1/2}$ the corresponding Lorentz factor (for simplicity, we omit the index in the velocities).

The moment equations are obtained by multiplying Eq. (B2) by powers of the four-velocity \mathbf{u} and integrating over \mathbf{u} -space. In particular, the first moment of the relativistic Vlasov equation yields the continuity equation

$$\partial_t \int d^3 u f_a + \nabla \cdot \int d^3 u \frac{\mathbf{u}}{\gamma} f_a = \partial_t n_a + \nabla \cdot (n_a \mathbf{V}_a) = 0, \quad (\text{B3})$$

while the second moment provides the momentum equation

$$m_a n_a (\partial_t \mathbf{U}_a + \mathbf{V}_a \cdot \nabla \mathbf{U}_a) + \nabla \cdot \mathbf{P}_a = q_a n_a (\mathbf{E} + \mathbf{V}_a \times \mathbf{B}), \quad (\text{B4})$$

where the pressure tensor \mathbf{P}_a is defined solely in terms of thermal inertia effects

$$\begin{aligned} \mathbf{P}_a &:= \int d^3 u m_a \frac{\mathbf{u} \mathbf{u}}{\gamma} f_a - m_a n_a \mathbf{V}_a \mathbf{U}_a \\ &= \mathbf{\Pi}_a - m_a n_a \mathbf{V}_a \mathbf{U}_a. \end{aligned} \quad (\text{B5})$$

Multiplying the continuity equation by $m_a \mathbf{U}_a$ and substituting into Eq. (B4) after using the vector identity $n_a \mathbf{V}_a \cdot \nabla \mathbf{U}_a = \nabla \cdot (n_a \mathbf{V}_a \mathbf{U}_a) - \mathbf{U}_a \nabla \cdot (n_a \mathbf{V}_a)$ yields a more convenient form

$$\begin{aligned} m_a \left[\frac{\partial}{\partial t} (n_a \mathbf{U}_a) + \nabla \cdot (n_a \mathbf{V}_a \mathbf{U}_a) \right] + \nabla \cdot \mathbf{P}_a - \\ q_a n_a (\mathbf{E} + \mathbf{V}_a \times \mathbf{B}) = 0. \end{aligned} \quad (\text{B6})$$

Noting that the inertial term in the first line of Eq. (B6) cancels with the contribution from the pressure tensor (B5), we obtain the following, more compact form of the momentum equation or, equivalently, of Ohm's law

$$m_a \frac{\partial}{\partial t} (n_a \mathbf{U}_a) + \nabla \cdot \mathbf{\Pi}_a - q_a n_a (\mathbf{E} + \mathbf{V}_a \times \mathbf{B}) = 0, \quad (\text{B7})$$

where the distinction between inertial and thermal effects is lost.

To derive the expression for the electric field, we apply this formulation to all plasma species by multiplying each equation by q_a/m_a so as to obtain the following set of equations

$$\begin{aligned} \frac{\partial}{\partial t} (en_+ \mathbf{U}_+) + \frac{e}{m_-} \nabla \cdot \mathbf{\Pi}_+ - \frac{e^2 n_+}{m_-} (\mathbf{E} + \mathbf{V}_+ \times \mathbf{B}) &= 0, \\ \frac{\partial}{\partial t} (en_- \mathbf{U}_-) + \frac{e}{m_-} \nabla \cdot \mathbf{\Pi}_- + \frac{e^2 n_-}{m_-} (\mathbf{E} + \mathbf{V}_- \times \mathbf{B}) &= 0, \\ \frac{\partial}{\partial t} (en_p \mathbf{U}_p) + \frac{e}{m_p} \nabla \cdot \mathbf{\Pi}_p - \frac{e^2 n_p}{m_p} (\mathbf{E} + \mathbf{V}_p \times \mathbf{B}) &= 0. \end{aligned} \quad (\text{B8})$$

Summing them to obtain the displacement momentum current density and solving for the electric field yields

$$\begin{aligned} \mathbf{E} &= \frac{m_-}{e^2 \mathcal{N}} \partial_t \mathcal{J} - \frac{1}{\mathcal{N}} (n_+ \mathbf{V}_+ + n_- \mathbf{V}_-) \times \mathbf{B} \\ &\quad - \frac{1}{\mathcal{N}} n_p \mathbf{V}_p \times \mathbf{B} - \frac{1}{e \mathcal{N}} \nabla \cdot \mathbf{\Pi}_- + \frac{1}{e \mathcal{N}} \nabla \cdot \mathbf{\Pi}_+ \\ &\quad + \frac{m_-}{m_p} \frac{1}{e \mathcal{N}} \nabla \cdot \mathbf{\Pi}_p, \end{aligned} \quad (\text{B9})$$

where we recall that $\mathcal{N} := n_p m_- / m_p + n_+ + n_-$ and $\mathcal{J} := \sum_a q_a n_a \mathbf{U}_a$. Expression (B9) clearly coincides Eq. (4) in the main text.

C. APPENDIX C: ADDITIONAL STATISTICS

Finally, we present in Fig. A3 information complementary to that in Fig. 3 of the main text, and report the PDF of the

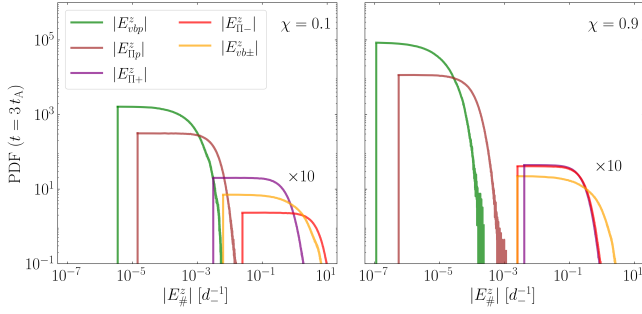


Figure A3. The same as in Fig. 3 but for $\chi = 0.1$ (left) and $\chi = 0.9$ (right). Much of what discussed for the case $\chi = 0.5$ in Fig. 3 applies also for the other concentrations.

various terms contributing to the z component of the electric field at $t = 3t_A$, computed over the whole domain. In contrast to Fig. 3, which was computed for $\chi = 0.5$, the panels in Fig. A3 refer to plasmas with $\chi = 0.1$ (left) and $\chi = 0.9$ (right), respectively.

A rapid comparison among the different cases highlights a behavior we have already emphasized. The almost pure electron-proton plasma ($\chi = 0.1$) produces sizeable contributions to the PDFs of the electromotive and pressure-gradient components of the electric field, i.e., E_{vbp}^z and $E_{\Pi p}^z$, respectively. Their strength, however, is subdominant and this is also true when considering an almost pure electron-positron plasma ($\chi = 0.9$). Hence, for all values of χ , the dominant contributions to the electric field come from the electron-positron electromotive component $E_{vb\pm}^z$ and the pressure-gradient terms $E_{\Pi+}^z$ and $E_{\Pi-}^z$. The latter satisfy $E_{\Pi-}^z \gtrsim E_{\Pi+}^z$ for $\chi = 0.1$ and $E_{\Pi-}^z \sim E_{\Pi+}^z$ for $\chi = 0.9$, as expected.

Finally, we comment on another widely used method to compute the reconnection rate at each X-point is to employ the plasma drift velocity in the vicinity of the reconnection site (see, e.g., El Mellah et al. 2022), which here we model as

$$\langle \mathcal{R}_{XP} \rangle := \langle |\mathbf{E} \times \mathbf{B}|_{\hat{n}} / (B_{\hat{n}}^2 + B_{\hat{t}}^2) \rangle_{XP}. \quad (\text{C10})$$

Ideally, our expectation was that the reconnection rate computed via Eq. (C10) would yield a statistics similar to that encountered with Eq. (C10) and shown in Fig. A2. In reality, we found that besides being less robust, the use of the drift velocity yields almost uniform PDFs of $\langle \mathcal{R}_{XP} \rangle$, thus making it difficult to determine a median value. This results suggests that the use of the drift velocity may be useful in highly magnetized plasmas, i.e., with $\sigma \gg 1$, where the motion of particles is constrained to follow the magnetic-field lines and the dynamics can be well approximated by the frozen-in field regime. Under these conditions, the drift velocity represents the transport velocity of the magnetic field lines and can provide a local estimate of the reconnection rate. However, in scenarios like the one explored here, where $\sigma \approx 1$ and turbulence is fully developed, the drift velocity also acquires a stochastic nature. Plasma inertia is comparable to, or even exceeds, the magnetic tension forces, and the local dynamics is dominated by effects such as compression, misalignments between \mathbf{E} and \mathbf{B} , instabilities (e.g., drift-kink), and pressure anisotropies. In this context, the quantity $\mathbf{E} \times \mathbf{B} / B^2$ can increase significantly near local minima of B^2 , as often occurs at X-points, leading to physically unreliable estimates of the reconnection rate. Overall, these results suggest that while reconnection rates may and should be estimated via multiple different methods, not all of them are equally adequate.

REFERENCES

- Adhikari, S., Shay, M. A., Parashar, T. N., et al. 2023, *Physics of Plasmas*, 30
- Alexandrova, O., Saur, J., Lacombe, C., et al. 2009, *Phys. Rev. Lett.*, 103, 165003
- Anderson, M., Hirschmann, E. W., Lehner, L., et al. 2008, *Phys. Rev. Lett.*, 100, 191101, doi: [10.1103/PhysRevLett.100.191101](https://doi.org/10.1103/PhysRevLett.100.191101)
- Balbus, S. A., & Hawley, J. F. 1998, *Reviews of modern physics*, 70, 1
- Bale, S. D., Kellogg, P. J., Mozer, F. S., Horbury, T. S., & Reme, H. 2005, *Phys. Rev. Lett.*, 94, 215002
- Ball, D., Sironi, L., & Özel, F. 2018, *Astrophys. J.*, 862, 80
- Bessho, N., & Bhattacharjee, A. 2005, *Phys. Rev. Lett.*, 95, 245001
- Biskamp, D. 2003, *Magnetohydrodynamic turbulence* (Cambridge University Press)
- Blandford, R., & Eichler, D. 1987, *Physics Reports*, 154, 1
- Blandford, R. D., & Payne, D. G. 1982, *Monthly Notices of the Royal Astronomical Society*, 199, 883–903
- Blandford, R. D., & Znajek, R. L. 1977, *Monthly Notices of the Royal Astronomical Society*, 179, 433–456
- Boris, J. P., & Shanny, R. A. 1973, *Proceedings (Naval Research Laboratory)*
- Camilloni, F., & Rezzolla, L. 2025, *Astrophys. J. Lett.*, 982, L31, doi: [10.3847/2041-8213/adbbef](https://doi.org/10.3847/2041-8213/adbbef)
- Cercignani, C., Kremer, G. M., Cercignani, C., & Kremer, G. M. 2002, *The relativistic boltzmann equation: Theory and applications*, 31
- Cerutti, B., Werner, G. R., Uzdensky, D. A., & Begelman, M. C. 2013, *Astrophys. J.*, 770, 147
- Comisso, L., & Sironi, L. 2018, *Phys. Rev. Lett.*, 121, 255101
- El Mellah, I., Cerutti, B., Crinquand, B., & Parfrey, K. 2022, *Astron. Astrophys.*, 663, A169
- Etienne, Z. B., Paschalidis, V., Haas, R., Mösta, P., & Shapiro, S. L. 2015, *Classical and Quantum Gravity*, 32, 175009

- Giacomazzo, B., & Rezzolla, L. 2007, *Class. Quantum Grav.*, 24, 235, doi: [10.1088/0264-9381/24/12/S16](https://doi.org/10.1088/0264-9381/24/12/S16)
- Giacomazzo, B., Rezzolla, L., & Baiotti, L. 2009, *Mon. Not. R. Astron. Soc.*, 399, L164, doi: [10.1111/j.1745-3933.2009.00745.x](https://doi.org/10.1111/j.1745-3933.2009.00745.x)
- González, C., Parashar, T., Gomez, D., Matthaeus, W., & Dmitruk, P. 2019, *Physics of Plasmas*, 26
- Harding, A. K., & Lai, D. 2006, *Reports on Progress in Physics*, 69, 2631
- Hesse, M., & Zenitani, S. 2007, *Physics of Plasmas*, 14
- Imbrogno, M., Meringolo, C., Servidio, S., et al. 2024, *Astrophys. J. Letters*, 972, L5
- Kagan, D., Sironi, L., Cerutti, B., & Giannios, D. 2015, *Space science reviews*, 191, 545
- Kiuchi, K., Reboul-Salze, A., Shibata, M., & Sekiguchi, Y. 2024, *Nature Astronomy*, 8, 298, doi: [10.1038/s41550-024-02194-y](https://doi.org/10.1038/s41550-024-02194-y)
- Komissarov, S. S., Barkov, M. V., Vlahakis, N., & Königl, A. 2007, *Monthly Notices of the Royal Astronomical Society*, 380, 51
- Kumar, P., & Zhang, B. 2015, *Physics Reports*, 561, 1
- Lewis, H. C., Stawarz, J. E., Franci, L., et al. 2023, *Physics of Plasmas*, 30
- Liboff, R. L. 2003, *Kinetic theory: classical, quantum, and relativistic descriptions* (Springer Science & Business Media)
- Liska, M., Tchekhovskoy, A., & Quataert, E. 2020, *Monthly Notices of the Royal Astronomical Society*, 494, 3656
- Liu, Y.-H., Guo, F., Daughton, W., Li, H., & Hesse, M. 2015, *Physical Review Letters*, 114, 095002
- McKinney, J. C. 2006, *Monthly Notices of the Royal Astronomical Society*, 368, 1561
- Meringolo, C., Cruz-Osorio, A., Rezzolla, L., & Servidio, S. 2023, *Astrophys. J.*, 944, 122
- . 2025, in preparation
- Meringolo, C., Pucci, F., Nisticó, G., et al. 2024, *A&A*, 688, A12, doi: [10.1051/0004-6361/202349094](https://doi.org/10.1051/0004-6361/202349094)
- Most, E. R., & Quataert, E. 2023, *Astrophys. J. Lett.*, 947, L15, doi: [10.3847/2041-8213/acca84](https://doi.org/10.3847/2041-8213/acca84)
- Mösta, P., Mundim, B. C., Faber, J. A., et al. 2013, *Classical and Quantum Gravity*, 31, 015005
- Murray, N., Chiang, J., Grossman, S., & Voit, G. 1995, *Astrophysical Journal* v. 451, p. 498, 451, 498
- Musolino, C., Rezzolla, L., & Most, E. R. 2024, arXiv e-prints, arXiv:2410.06253, doi: [10.48550/arXiv.2410.06253](https://doi.org/10.48550/arXiv.2410.06253)
- Nathanail, A., Fromm, C. M., Porth, O., et al. 2020, *Mon. Not. R. Astron. Soc.*, 495, 1549, doi: [10.1093/mnras/staa1165](https://doi.org/10.1093/mnras/staa1165)
- Nathanail, A., Mpisketis, V., Porth, O., Fromm, C. M., & Rezzolla, L. 2022, *Mon. Not. R. Astron. Soc.*, 513, 4267, doi: [10.1093/mnras/stac1118](https://doi.org/10.1093/mnras/stac1118)
- Nathanail, A., Mpisketis, V., Porth, O., Fromm, C. M., & Rezzolla, L. 2022, *Monthly Notices of the Royal Astronomical Society*, 513, 4267
- Palenzuela, C., Lehner, L., Reula, O., & Rezzolla, L. 2009, *Monthly Notices of the Royal Astronomical Society*, 394, 1727
- Parker, E. N. 1957, *Journal of Geophysical Research*, 62, 509
- Phan, T., Eastwood, J. P., Shay, M., et al. 2018, *Nature*, 557, 202
- Philippov, A., & Kramer, M. 2022, *Annual Review of Astronomy and Astrophysics*, 60, 495
- Piran, T. 2004, *Reviews of modern physics*, 76, 1143
- Porth, O., Olivares, H., Mizuno, Y., et al. 2017, *Computational Astrophysics and Cosmology*, 4, 1
- Porth, O., Chatterjee, K., Narayan, R., et al. 2019, *Astrophys. J. Supp.*, 243, 26, doi: [10.3847/1538-4365/ab29fd](https://doi.org/10.3847/1538-4365/ab29fd)
- Proga, D., Stone, J. M., & Kallman, T. R. 2000, *Astrophys. J.*, 543, 686
- Ressler, S. M., Quataert, E., White, C. J., & Blaes, O. 2021, *Monthly Notices of the Royal Astronomical Society*, 504, 6076
- Rezzolla, L., & Zanotti, O. 2013, *Relativistic Hydrodynamics* (Oxford University Press), doi: [10.1093/acprof:oso/9780198528906.001.0001](https://doi.org/10.1093/acprof:oso/9780198528906.001.0001)
- Ripperda, B., Bacchini, F., & Philippov, A. A. 2020, *Astrophys. J.*, 900, 100
- Rowan, M. E., Sironi, L., & Narayan, R. 2017, *Astrophys. J.*, 850, 29, doi: [10.3847/1538-4357/aa9380](https://doi.org/10.3847/1538-4357/aa9380)
- Sahraoui, F., Goldstein, M. L., Robert, P., & Khotyaintsev, Y. V. 2009, *Phys. Rev. Lett.*, 102, 231102
- Servidio, S., Matthaeus, W., Shay, M., et al. 2010, *Physics of Plasmas*, 17
- Servidio, S., Matthaeus, W. H., Shay, M. A., Cassak, P. A., & Dmitruk, P. 2009, *Phys. Rev. Lett.*, 102, 115003
- Servidio, S., Valentini, F., Califano, F., & Veltri, P. 2012, *Phys. Rev. Lett.*, 108, 045001
- Sharma Pyakurel, P., Shay, M., Phan, T., et al. 2019, *Physics of Plasmas*, 26
- Shibata, M., & Sekiguchi, Y.-i. 2005, *Physical Review D—Particles, Fields, Gravitation, and Cosmology*, 72, 044014
- Sironi, L., Giannios, D., & Petropoulou, M. 2016, *Monthly Notices of the Royal Astronomical Society*, 462, 48
- Sironi, L., Petropoulou, M., & Giannios, D. 2015, *Monthly Notices of the Royal Astronomical Society*, 450, 183
- Sironi, L., & Spitkovsky, A. 2014, *Astrophys. J. Letters*, 783, L21
- Tchekhovskoy, A., Narayan, R., & McKinney, J. C. 2011, *Monthly Notices of the Royal Astronomical Society: Letters*, 418, L79
- Uzdensky, D. A., & Loureiro, N. F. 2016, *Physical Review Letters*, 116, 105003
- Vos, J., Cerutti, B., Moscibrodzka, M., & Parfrey, K. 2024, arXiv preprint arXiv:2410.19061
- Yamada, M., Kulsrud, R., & Ji, H. 2010, *Reviews of modern physics*, 82, 603
- Zenitani, S., & Hoshino, M. 2001, *Astrophys. J.*, 562, L63